

Dynamics of driven three-dimensional thin films: From hydrophilic to superhydrophobic regimes

R. Ledesma-Aguilar,^{1,a)} A. Hernández-Machado,¹ and I. Pagonabarraga²

¹Departament d'Estructura i Constituents de la Matèria, Universitat de Barcelona, Avinguda Diagonal 647, E-08028 Barcelona, Spain

²Departament de Física Fonamental, Universitat de Barcelona, Avinguda Diagonal 647, E-08028 Barcelona, Spain

(Received 23 January 2008; accepted 19 May 2008; published online 10 July 2008)

We study the forced displacement of a thin film of fluid in contact with vertical and inclined substrates of different wetting properties, that range from hydrophilic to hydrophobic, using the lattice-Boltzmann method. We study the stability and pattern formation of the contact line in the hydrophilic and superhydrophobic regimes, which correspond to wedge-shaped and nose-shaped fronts, respectively. We find that contact lines are considerably more stable for hydrophilic substrates and small inclination angles. The qualitative behavior of the front in the linear regime remains independent of the wetting properties of the substrate as a single dispersion relation describes the stability of both wedges and noses. Nonlinear patterns show a clear dependence on wetting properties and substrate inclination angle. The effect is quantified in terms of the pattern growth rate, which vanishes for the sawtooth pattern and is finite for the finger pattern. Sawtooth shaped patterns are observed for hydrophilic substrates and low inclination angles, while finger-shaped patterns arise for hydrophobic substrates and large inclination angles. Finger dynamics show a transient in which neighboring fingers interact, followed by a steady state where each finger grows independently. © 2008 American Institute of Physics. [DOI: 10.1063/1.2940726]

I. INTRODUCTION

The stability of forced contact lines is the key to a variety of dynamic wetting processes^{1,2} that range from linear or spin coating of surfaces³ to monodisperse drop formation⁴ and in-drop mixing in microchannels.^{5,6}

In this paper we study the dynamics of a three-dimensional thin film spreading on a dry inclined substrate, where the contact line is gravity driven, as shown in Fig. 1. In such a case, the contact line destabilizes and gives rise to the growth of differently shaped patterns.

The stability of the front has been subject of active work during the last two decades. Experimentally, efforts have focused on characterizing the destabilization of the contact line and the patterns that emerge at long times. Patterns have been shown to be influenced by fluid wetting properties. Silvi and Dussan⁷ already observed such a dependence, as patterns in their experiments ranged from sawtooth shaped for mostly wetting fluids to finger shaped for mostly nonwetting fluids. This feature was verified in the experimental work of Jerret and de Bruyn,⁸ who found that the width of the pattern is a function of the wetting properties as well as of the imposed forcing, i.e., the inclination angle of the substrate. In general, experiments indicate that closely spaced patterns are expected for mostly wetting fluids at small inclination angles.

Theoretically, the main framework is that of the lubrication approximation of the Navier–Stokes equations, subject to some boundary condition at the moving contact line that

regularizes the so-called viscous dissipation singularity.² In the lubrication approximation one reduces the dynamics of the thin film to a two-dimensional evolution equation for the film thickness h , which is governed by a single parameter $D=(3Ca)^{1/3} \cot(\alpha)$, where Ca is the capillary number and α is the inclination angle of the substrate. Wetting properties are fixed by the choice of the boundary condition at the contact line, which generally corresponds to perfectly wetting fluids, where the dynamic contact angle θ_D is zero (precursor film model), or to mostly wetting fluids, where θ_D is small (slip model).

The lubrication equations were first examined qualitatively by Brenner,⁹ who proposed that the capillary ridge located near the contact line (a consequence of the competition between capillary and driving forces) induces transverse flows that destabilize the contact line when it is perturbed. Troian *et al.*¹⁰ solved numerically the linear stability problem in the long-wavelength limit using a precursor film model for the contact line. Indeed, they found that the perturbation growth rate can only be positive if the height profile is non-monotonic. Bertozzi and Brenner¹¹ extended the linear stability analysis to arbitrary wavelengths using the same contact line model finding similar results. Spaid and Homsy¹² compared the stability of the front for the precursor film model and the slip model. They found that the front is rather insensitive to the contact line model used and that the front stability is very similar whenever the precursor film thickness and the slip length are comparable. Anyhow, all studies agree on the destabilization mechanism, which is based on transverse variations of the height profile in the presence of a capillary ridge. In this situation, the troughs of a perturbation

^{a)}Electronic mail: rodrigo@ecm.ub.es.

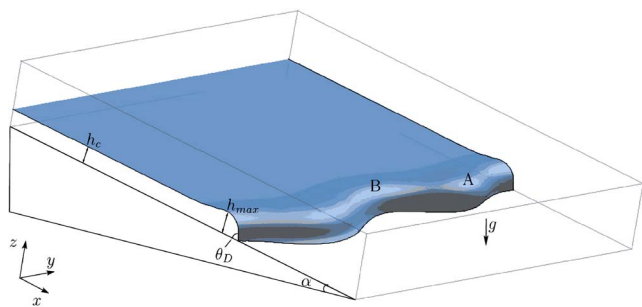


FIG. 1. (Color online) Thin film flowing down an inclined plane. The height of the film h is constant and equal to h_c in the upstream region while it bends into a ridge close to the contact line, where it meets the solid with a dynamic contact angle θ_D . The maximum height of the film $h_{\max}(y)$ determines the size of the ridge. Upon a perturbation of the contact line, the ridge varies spatially. Points A and B correspond to the peak and the trough of the perturbation. Relaxation of the ridge at point B tends to feed mass to point A , therefore generating a destabilization mechanism.

feed the peaks (points B and A in Fig. 1, respectively). As a consequence, the peaks increase their local height and, in turn, their velocity. In other words, a given value of the control parameter fixes the *size* of the capillary ridge and, in turn, the stability of the front.

The long time evolution of the lubrication equations has been addressed numerically by Kondic and Diez¹³ for completely wetting fluids and by Moyle *et al.*¹⁴ for partially wetting fluids. Kondic and Diez studied the effect of the inclination angle α and observed the formation of fingers at large α , while for sufficiently small inclination angle the growth of the pattern saturates to a sawtooth shape. Moyle *et al.*¹⁴ focused on the effect of the capillary number and dynamic contact angle on the shape of fingers. For small Ca and θ_D they observe sawtooth shaped patterns, while for larger values of both parameters they observe the growth of fingers.

In spite of these results, there are a number of situations that fall beyond the small- Ca and small- θ_D limit of lubrication theory.

Concerning the role of large θ_D , an interesting effect was observed by Veretennikov *et al.*,¹⁵ who considered the flow of films of partially wetting fluids at small inclination angles. Instead of the wedge shaped front typical of lubrication theory, they observe a multivalued film thickness profile; a nose shaped front, where the flow is no longer unidirectional, but has a vortex structure. This three-dimensional limit is typical of the hydrophobic ($\theta_D > 90^\circ$) and superhydrophobic ($\theta_D > 120^\circ$) regimes.

Alternatively to lubrication theory, three-dimensional flows of immiscible fluids can be modeled by a mesoscopic version of the Navier–Stokes equations coupled to a convection-diffusion equation for an order parameter. Such an approach has been used by a number of authors in fields as varied as spinodal decomposition¹⁶ and shearing¹⁷ of binary fluids, contact line motion between sheared solid plates,¹⁸ and viscous fingering in Hele–Shaw cells.^{19,20} Under this approach, the contact line and the free film surface have a finite size, a feature that eliminates the complications of a sharp interface. Additionally, the evolution equation of the order parameter can be constructed from a well-known

equilibrium state, thus allowing for a correct description of wetting properties. In our model, wetting is introduced by considering a surface free energy of the Cahn type, which fixes a boundary condition for the order parameter field at the solid.

In this paper we perform numerical simulations of the mesoscopic Navier–Stokes and convection-diffusion equations to study the full three-dimensional problem of a thin film flowing down a dry inclined substrate using the lattice-Boltzmann method. We focus mainly on situations in which neither Ca nor θ_D are small, so the lubrication equations are no longer valid. We consider fluids of arbitrary wetting properties at various inclination angles. We study in detail the unperturbed front by characterizing the wedge and nose configurations. We then study the stability of these solutions where we pay particular attention to the effect of wetting properties. For long periods, we study the formation of nonlinear patterns. We find that, depending on the wetting properties and the inclination angle, saturated sawtooth patterns or steadily growing fingers are obtained, and subsequently study the robustness of the finger pattern.

The present paper is organized as follows. In Sec. II we present the three-dimensional model which consists of the coupled Navier–Stokes and convection-diffusion equations subject to a Cahn wetting boundary condition. We discuss the lubrication limit of these equations. In Secs. III and IV we present the lattice-Boltzmann method and the simulation strategy, respectively. The flat contact line problem is addressed in Sec. V, where we explore the effects of wetting, capillarity, and gravity on a propagating front. In Sec. VI we perform a numerical linear stability analysis for a slightly perturbed contact line. We explore the effect of wetting and gravity and compare to previous results.¹² In Sec. VII we study the nonlinear regime of contact line dynamics. In Sec. VII A we study the growth of sawtooth patterns and fingers, which is controlled either by varying substrate wettability or substrate inclination angle. Finger growth is studied in detail in Sec. VII B, where we consider the effect of initial conditions, system size, and nonlinear interaction between neighboring fingers. In Sec. VIII we discuss our results and present the conclusions of this work.

II. GOVERNING EQUATIONS

We consider the motion of a thin film of fluid that flows down an inclined solid substrate under the action of gravity, as depicted in Fig. 1. We consider a binary fluid composed of two immiscible phases of very different viscosities. In this approximation, the more viscous fluid plays the role of the film, while the less viscous fluid plays the role of the surrounding air. Each phase is determined by a dimensionless composition variable, or order parameter, $\phi(\vec{r})$. In equilibrium, ϕ minimizes a free energy functional given by

$$\mathcal{F}\{\rho, \phi\} = \int d\vec{r} \left[V(\phi, \rho) + \frac{\kappa}{2} (\nabla \phi)^2 \right],$$

where $\rho(\vec{r})$ is the fluid density. The first term in the integrand, $V(\phi, \rho) = A\phi^2/2 + B\phi^4/4 + \rho \ln \rho$, is a volume contribution and determines the equilibrium composition values for each

phase, while the second term penalizes composition gradients by a factor κ , thus defining the free energy of the interface.

Minimization of \mathcal{F} leads to the chemical potential,

$$\mu = \partial_\phi V - \kappa \nabla^2 \phi,$$

and total pressure tensor,

$$\bar{\bar{P}}_T = \left[\frac{\rho}{3} + \phi \partial_\phi V - V - \kappa \left(\phi \nabla^2 \phi + \frac{1}{2} |\vec{\nabla} \phi|^2 \right) \right] \bar{\bar{\delta}} + \kappa \vec{\nabla} \phi \vec{\nabla} \phi,$$

where $\bar{\bar{\delta}}$ is the diagonal matrix. The pressure tensor has an ideal contribution given by $\bar{\bar{P}} = (\rho/3) \bar{\bar{\delta}}$, and an order parameter contribution. The equilibrium order parameter profile is $\phi^*(n) = -\phi_{\text{eq}} \tanh(n/\xi)$, where $\phi_{\text{eq}} = (-A/B)^{1/2}$ is the bulk equilibrium value of the order parameter, $\xi = (-\kappa/2A)^{1/2}$ is the length scale of the interfacial region, and n is a coordinate that measures the distance from the interface in the normal direction. The energy per unit area of the interface is $\sigma = (-8\kappa A^3/9B^2)^{1/2}$.

The divergence of the pressure tensor yields the force per unit volume that acts on the fluid: $-\vec{\nabla} P - \phi \vec{\nabla} \mu$. The first term is the pressure gradient, while the second arises from order parameter inhomogeneities. Including this last term, the Navier–Stokes equations are written as follows:

$$\rho(\partial_t \vec{v} + \vec{v} \cdot \vec{\nabla} \vec{v}) = -\vec{\nabla} P - \phi \vec{\nabla} \mu + \eta \nabla^2 \vec{v} + \rho \vec{g}, \quad (1)$$

where \vec{v} is the fluid velocity, η is the fluid viscosity, and \vec{g} is the acceleration of gravity.

The dynamics of the order parameter are described by a convection-diffusion equation,

$$\partial_t \phi + \vec{v} \cdot \vec{\nabla} \phi = M \nabla^2 \mu, \quad (2)$$

where M is a mobility. For small deviations from the equilibrium configuration, an expansion of the chemical potential in powers of $\phi - \phi^*$ yields a first-order diffusion coefficient $D_\phi = M(A + 3B\phi_{\text{eq}}^2)$.

In the sharp interface limit ($\epsilon \rightarrow 0$) Eq. (1) reduces to the usual Navier–Stokes equations in the bulk of each fluid, while at the interface the Gibbs–Thomson condition is recovered. In addition, for low D_ϕ , the diffusive term in Eq. (2) vanishes. Consequently, the order parameter is advected by the velocity field.

In this limit, the standard approach of previous works^{9–14} is to restrict the equations to the lubrication regime, which follows by considering only the components of the equations of motion parallel to the solid substrate averaged over the film thickness, $h(x, y)$. Consequently, the local fluid velocity is given by

$$\langle \vec{v} \rangle = -\frac{h^2}{3\eta} [\vec{\nabla} P - \rho g \sin(\alpha) \hat{t}], \quad (3)$$

where the x -component of the gravitational force comes from the choice of the reference frame (see Fig. 1). In Eq. (3), the local pressure is composed of a surface term and a hydrostatic term, $P = -\sigma \nabla^2 h + \rho g h \cos(\alpha)$. The local velocity is

then a function of the local height and of its spatial derivatives.

Averaging the continuity equation over h and combining with Eq. (3) give a fourth-order partial differential equation for the film thickness, which is the main equation in lubrication theory,

$$\frac{\partial h}{\partial t} = -\frac{1}{3\eta} \vec{\nabla} \cdot [\sigma h^3 \vec{\nabla} \nabla^2 h - \rho g h^3 \vec{\nabla} \cos(\alpha) + \rho g h^3 \sin(\alpha) \hat{t}]. \quad (4)$$

This equation can be nondimensionalized by using units $h' = h/h_c$, $(x', y') = (x/x_c, y/x_c)$, and $t' = t/t_c$, where h_c is the film height far from the contact line. Space and time units are chosen as $x_c = h_c(3\text{Ca})^{-1/3}$ and $t_c = x_c/U$, where $\text{Ca} = \eta U/\sigma$ is the capillary number and $U = h_c^2 \rho g \sin(\alpha)/3\eta$ is the average velocity of the film. In terms of the nondimensional variables Eq. (4) becomes

$$\frac{\partial h'}{\partial t'} = -\vec{\nabla}' \cdot [h'^3 \vec{\nabla}' \nabla'^2 h' - D h'^3 \vec{\nabla}' h' + h'^3 \hat{t}'], \quad (5)$$

where $D = (3\text{Ca})^{1/3} \cot(\alpha)$ measures the magnitude of the normal gravitational force. According to lubrication theory, D is the only relevant control parameter of the system.

A. Boundary conditions

Wetting properties in the mesoscopic model presented above are included by means of an interaction energy between the fluid and the solid

$$F_S = \int_S dS f_S(\phi_S),$$

where S is the solid-fluid boundary and $f_S(\phi_S)$ is the free energy per unit surface, which is a function of the local composition ϕ_S . In equilibrium this expression yields the following boundary condition at the solid-fluid interface:

$$|\vec{\nabla} \phi \cdot \hat{n}| = \frac{1}{\kappa} \frac{df_S}{d\phi_S}, \quad (6)$$

where \hat{n} is normal to the boundary. Here we consider a linear form for the surface free energy density, $f_S = H\phi_S$, which already allows a wetting transition.²¹

For a rectangular box of dimensions $L \times W \times b$, stick boundary conditions are imposed at the solid, $\vec{v}(x, y, z=0) = \vec{0}$, while no flow boundary conditions are imposed for the order parameter, $\phi \vec{v}(x, y, z=0) = \vec{0}$. Far above from the film and at both ends of the box the flow is homogeneous. We ensure these conditions by fixing $\partial_z \rho \vec{v}(x, y, z=b) = \partial_z \phi \vec{v}(x, y, z=b) = \vec{0}$, $\partial_x \rho \vec{v}(x=0, y, z) = \partial_x \rho \vec{v}(x=L, y, z) = \vec{0}$, and $\partial_x \phi \vec{v}(x=0, y, z) = \partial_x \phi \vec{v}(x=L, y, z) = \vec{0}$. Periodic boundary conditions are applied in the y direction.

Contact line dynamics arise from the diffuse nature of the interface, which allows for slip in the interfacial region by a diffusive mechanism. The size over which slip takes place, l_D , is a function of the fluid properties and has been estimated by Briant and Yeomans,¹⁸ who have given a scaling relation, $l_D \sim (\eta \xi^2 M / \Delta \phi^2)^{1/4}$.

III. LATTICE-BOLTZMANN METHOD

We solve numerically Eqs. (1) and (2) by means of the lattice-Boltzmann algorithm presented in Ref. 16. The dynamics are introduced by discretized Boltzmann equations of two velocity distribution functions,

$$f_i(\vec{r} + \vec{c}_i, t + 1) - f_i(\vec{r}, t) = -\frac{1}{\tau_f}(f_i - f_i^{\text{eq}}) + F_i^f \quad (7)$$

and

$$g_i(\vec{r} + \vec{c}_i, t + 1) - g_i(\vec{r}, t) = -\frac{1}{\tau_g}(g_i - g_i^{\text{eq}}). \quad (8)$$

In these equations, f_i and g_i are velocity distribution functions of particles that move with velocity \vec{c}_i , where the index i counts over the model velocity set. Space is discretized as a cubic lattice where nodes are joined by velocity vectors. Space and time units in Eqs. (7) and (8) are set to unity. Likewise, the density of the fluids is set to one. We use the D3Q15 velocity set,²¹ which consists of 15 velocity vectors: six of magnitude 1 that correspond to nearest neighbors, eight of magnitude $\sqrt{3}$ that correspond to third-nearest neighbors, and one of zero magnitude that accounts for rest particles. In the D3Q15 model the speed of sound is $c_s = 1/\sqrt{3}$. In Eqs. (7) and (8), distribution functions are first relaxed to equilibrium values, represented by f_i^{eq} and g_i^{eq} , with relaxation time scales τ_f and τ_g . The term F_i^f is related to the external forcing. Following the collision stage, distribution functions are propagated to neighboring sites.

Hydrodynamic variables are defined through moments of the f_i and g_i ; the local density and order parameter are introduced as $\sum_i f_i = \rho$ and $\sum_i g_i = \phi$. The fluid momentum is defined as $\sum_i f_i \vec{c}_i = \rho \vec{v}$. Local conservation of mass and momentum is enforced through the conditions $\sum_i f_i^{\text{eq}} = \rho$, $\sum_i g_i^{\text{eq}} = \phi$, and $\sum_i f_i^{\text{eq}} \vec{c}_i = \rho \vec{v}$. In equilibrium, the order parameter current, pressure tensor and chemical potential are defined as $\sum_i g_i^{\text{eq}} \vec{c}_i = \phi \vec{v}$, $\sum_i f_i^{\text{eq}} \vec{c}_i \vec{c}_i = \rho \vec{v} \vec{v} + \bar{P}_T$, and $\sum_i g_i^{\text{eq}} \vec{c}_i \vec{c}_i = \hat{M} \mu \bar{\delta} + \phi \vec{v} \vec{v}$.

The equilibrium distribution functions and the forcing term are written as expansions in powers of \vec{v} ,²² i.e.,

$$f_i^{\text{eq}} = \rho \omega_\nu \left(A_\nu^f + 3\vec{v} \cdot \vec{c}_i + \frac{9}{2} \vec{v} \vec{v} : \vec{c}_i \vec{c}_i - \frac{3}{2} v^2 + \bar{G}^f : \vec{c}_i \vec{c}_i \right),$$

$$g_i^{\text{eq}} = \rho \omega_\nu \left(A_\nu^g + 3\vec{v} \cdot \vec{c}_i + \frac{9}{2} \vec{v} \vec{v} : \vec{c}_i \vec{c}_i - \frac{3}{2} v^2 + \bar{G}^g : \vec{c}_i \vec{c}_i \right),$$

and

$$F_i^f = 4\omega_\nu \left(1 - \frac{1}{2\tau_f} \right) [\vec{f} \cdot \vec{c}_i (1 + \vec{v} \cdot \vec{c}_i) - \vec{v} \cdot \vec{f}].$$

Here, ν stands for the three possible magnitudes of the \vec{c}_i set. Coefficient values are $\omega_0 = 2/9$, $\omega_1 = 1/9$, and $\omega_{\sqrt{3}} = 1/72$; $A_0^f = 9/2 - 7/2 \text{Tr} \bar{P}$, $A_1^f = A_{\sqrt{3}}^f = 1/\rho \text{Tr} \bar{P}$, and $\bar{G}^f = 9/(2\rho) \bar{P} - 3\bar{\delta} \text{Tr} \bar{P}$; $A_0^g = 9/2 - 21/2 \hat{M} \mu$, $A_1^g = A_{\sqrt{3}}^g = 3\hat{M} \mu / \rho$, and $\bar{G}^g = 9/(2\rho) \hat{M} \mu (\bar{1} - \bar{\delta})$, where $\bar{1}$ is the unit matrix.

Equations (1) and (2) are recovered by performing a Chapman–Enskog expansion of Eqs. (7) and (8).²³ The lattice-Boltzmann scheme maps to the hydrodynamic model through the relaxation time scales, i.e., $\eta = (2\tau_f - 1)/6$ and $M = (\tau_g - 1/2) \hat{M}$, and through the body force $\vec{f} = \rho \vec{g}$.

Solid boundaries in the lattice-Boltzmann method are implemented by means of the well-known bounce-back rules.^{21,23} In the fluid nodes that link to solid nodes, the propagation scheme is modified so the distribution functions are bounced back to the fluid rather than absorbed by the solid. As a consequence, a stick condition for the velocity is recovered approximately halfway from the fluid node to the solid node.

IV. SIMULATION SETUP AND MEASUREMENTS

Our aim is to study the flow of thin films for different Ca, α , and θ_E . To achieve this we must choose values for the model parameters that assure the numerical stability of the algorithm.

The typical experimental situation is that of the forced spreading of a viscous fluid on a substrate in the presence of air at relatively small velocities. Inertial effects, quantified by the Reynolds number $\text{Re} = \rho h_c U / \eta$, are expected to be small. This is enforced in our simulations by neglecting the nonlinear term in Eq. (1). The local viscosity is set according to the mixing rule $\eta(\phi) = (\eta + \eta_A)(1 + \phi / \phi_{\text{eq}}) / 2$, where $c = (\eta - \eta_A) / (\eta + \eta_A)$ is the viscosity contrast between the fluids and the subscript A stands for the less viscous phase. To reproduce the high asymmetry of viscous dissipation between both fluids, we fix $c = 0.9$, so viscous dissipation occurs mainly inside the film.

Given that we work with a finite-size interface, the ratio between the interfacial and macroscopic scales should be reasonably small so that bulk effects do not become shadowed by the interface structure. Still, the interface has to be sufficiently thick to avoid lattice artifacts. This is ensured by fixing $\epsilon = 0.57$ which is sufficiently large to resolve the interface.²¹ For this interface size, film dynamics is correctly resolved by taking $h \sim O(10)$.

As we have mentioned before, the contact line slips by virtue of diffusion. This means that the diffusion coefficient D_ϕ must be chosen to ensure that the order parameter relaxes rapidly compared to the advection time scale. In a previous study we have shown that this is accomplished as long as the product between the Péclet number $\text{Pe} = Uh / D_\phi$ and the capillary number is $O(10^{-1})$.¹⁹

After these considerations all other parameters are fixed by a choice of Ca, θ_E , and α . The corresponding velocity, viscosity, and surface tension lie in the ranges of $0.001 \leq U \leq 0.01$, $0.05 \leq \eta \leq 0.5$, and $0.001 \leq \sigma \leq 0.01$, respectively. The body force terms are fixed according to $g_x = 3\eta U(\phi + 1)/h^2$ and $g_z = -g_x \cot(\alpha)$. Then, choosing α fixes the capillary number. As for wetting properties, fixing θ_E determines the value of the wetting coefficient H .

Initial conditions are set by fixing the height h , length l , and width w of a rectangular film. Lattice nodes lying inside of the film are set to $\phi = \phi_{\text{eq}}$, while the rest of the nodes are set to $\phi = -\phi_{\text{eq}}$. The initial velocity of all nodes is set to $(U, 0, 0)$.

For a given configuration of the order parameter, a choice of an iso- ϕ curve determines the location of the interface. Here we choose the value $\phi = 0$. The dynamic contact angle is extracted by a circle fit to interface coordinates in

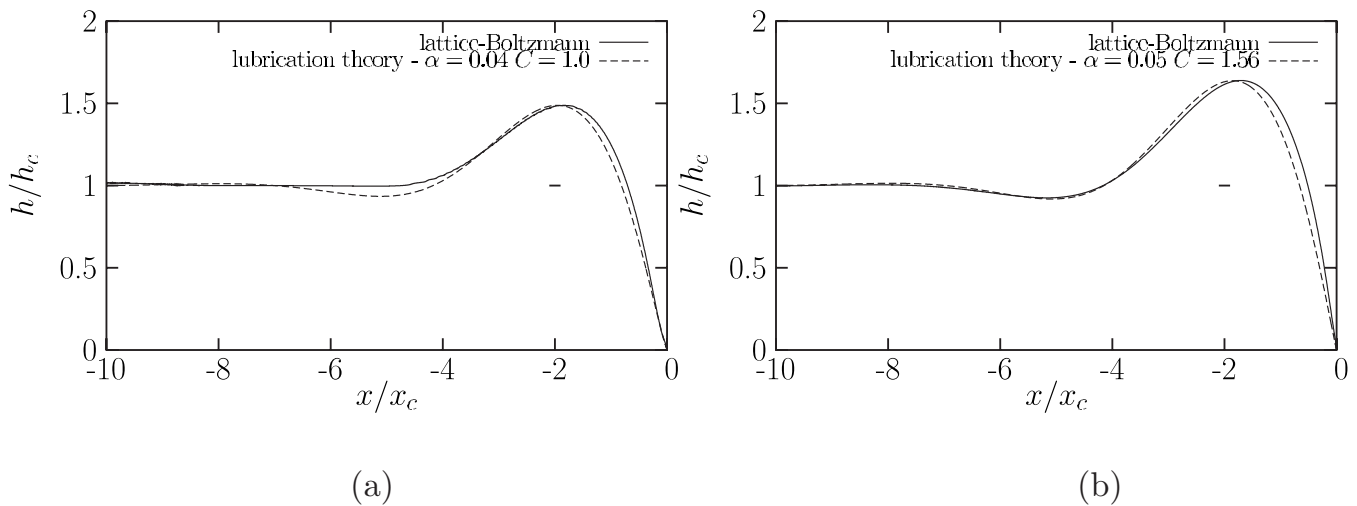


FIG. 2. Height profile comparison between lattice-Boltzmann and lubrication theory in the small Ca and θ_D limit. Parameter values are $D=0$, $Ca=0.041$, and $\theta_E=0^\circ$. (a) $D_\phi=0.074$ and $\theta_D=28^\circ$ and (b) $D_\phi=0.006$ and $\theta_D=48^\circ$. Deviations from the lubrication prediction are comparable to the size of the interface, represented by the black segment located in the ridge of each profile.

the xz -plane. To improve the accuracy, the fitting region is varied systematically by increasing the arc length along the interface until the fitting error becomes minimum. As is standard, we only consider the part of the interface that couples to bulk dynamics and discard the region close to the wall, where the profile distorts due to the wetting boundary condition²⁴ [see, for instance, Fig. 3(e)].

V. FLAT CONTACT LINE

Before exploring the stability and pattern formation of the thin film let us consider the effect of wetting properties on the evolution of an unperturbed front, for which the contact line is flat. Here we depart from the lubrication regime, in which the only parameter D gathers the effects of Ca and α . Apart from these parameters, we study fronts at three different equilibrium contact angles: $\theta_E=0^\circ$, $\theta_E=25^\circ$, and $\theta_E=90^\circ$.

A. Vertical substrates

Let us first examine the low Ca and low θ_D limit for a vertical substrate ($D=0$), which corresponds to the lubrication regime, and compare to lattice-Boltzmann results. We perform a simulation fixing $\theta_E=0^\circ$ and $Ca=0.04$. The resulting profile, shown in Fig. 2(a), has a dynamic contact angle of $\theta_D=28^\circ$. In our model, the contact line slips over the solid surface due the diffusive mechanism that originates from the finite-sized interface. Therefore, we choose to compare to the slip-velocity lubrication model of Ref. 12, which follows from coupling Eq. (5) to a slip boundary condition at the solid-fluid interface. For a flat, steady contact line, the height profile of such a model satisfies the equation

$$\frac{\partial^3 h'}{\partial x'^3} = 1 - \frac{1 + \alpha_h}{h'^2 + \alpha_h},$$

where α_h is the slip parameter. Typical values of this parameter used in Ref. 12 lie in the range of $0.01 \leq \alpha_h \leq 0.1$. Numerical solution of this equation is performed by fixing α_h ,

the contact slope $C=(3Ca)^{-1/3} \tan \theta_D$, and using a fourth order Runge–Kutta integration scheme. To compare to lattice-Boltzmann results, we vary α_h and C until a best fit of the lattice-Boltzmann profile is achieved. Figure 2(a) shows the comparison for $\alpha_h=0.04$ and $C=1.1$. Both profiles compare acceptably. Nonetheless, in the region behind the capillary ridge a characteristic “dip” is absent from the lattice-Boltzmann solution. To improve this comparison, we decrease the diffusion strength at the contact line, which is responsible for the slip velocity and, in turn, the strength of this dip. Decreasing this strength has the effect of increasing the contact slope slightly. Nonetheless, the resulting profile now compares better to the lubrication prediction with $\alpha_h=0.05$ and $C=1.56$, as can be seen in Fig. 2(b). In both cases, deviations are comparable to the size of the interface, as shown in the figure.

Let us now explore the effect of larger equilibrium contact angles at different Ca values. Plots of the steady free surface are shown in Fig. 3. Simulation parameters for these runs are summarized in Table I. For all runs the free surface relaxes to a steady state shape, consisting of a flat height profile that couples to a curved ridge near the contact line.

Profiles (a)–(e) in the figure correspond to $\theta_E=0^\circ$ and increasing Ca . The effect of Ca is to increase the curvature of the ridge, which in turn makes θ_D larger. This is also observed for runs (f)–(j) and (k)–(o), which correspond to $\theta_E=25^\circ$ and $\theta_E=90^\circ$, respectively. Measured contact angles are shown in Fig. 4 as a function of Ca . As seen in the plot, the profile changes from a wedge to a nose configuration by increasing the capillary number, even for $\theta_E=0^\circ$. As observed in experiments by Veretennikov *et al.*,¹⁵ the nose configuration has a multivalued height profile, a condition that is fulfilled only for $\theta_D > 90^\circ$. For sufficiently large Ca , we achieve contact angles as large as $\theta_D \approx 140^\circ$, a situation that renders the effective interaction between the wall and the fluid superhydrophobic.

Looking again at Fig. 3 we notice that Ca has an effect on the size of the capillary ridge, given by the maximum film

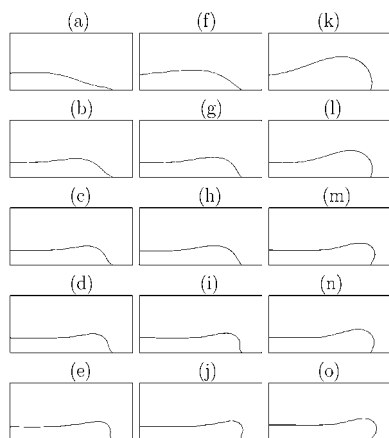


FIG. 3. Stationary xz -interface profiles for $D=0$ at various θ_E and Ca . The interface is defined by the isosurface $\phi=0$. The x - and z -scales are the same for all plots. Each column corresponds to a different equilibrium contact angle; from left to right: $\theta_E=0^\circ$, $\theta_E=25^\circ$, and $\theta_E=90^\circ$. For each column Ca increases downward (rows do not correspond to the same Ca value).

thickness h_{\max} and by the width over which h is larger than h_c (see Fig. 1). This effect is clearly different for hydrophilic and hydrophobic substrates. For a given Ca value, we observe thicker and wider ridges for hydrophobic substrates; runs (a), (f), and (k) were carried on at the same Ca value, still h_{\max} is approximately twice as large in run (k) than in runs (a) and (f). This tendency persists regardless of the value of the capillary number. Figure 5 shows plots of h_{\max} as a function of Ca for each contact angle considered. For $\theta_E=0^\circ$ and $\theta_E=25^\circ$ [Figs. 5(a) and 5(b)], h_{\max} has a weak dependence with Ca , while for $\theta_E=90^\circ$ [Fig. 5(c)], we find that h_{\max} decreases strongly as Ca increases. This effect is understood if we consider the limiting case of $Ca \rightarrow 0$, where the contact line is expected to recede due to an uncompensated Young force. As the contact line recedes the ridge grows without bound due to mass conservation.² A finite Ca adds a driving force to the picture. The ridge then grows until the driving force and the Young force is balanced by viscous stresses. Given that the Young force is larger for larger θ_E , the size of the ridge is expected to be larger for hydrophobic substrates.

We draw as a conclusion that the wetting properties of the substrate are relevant for the shape of the front. In contrast with lubrication theory, D is not the only control parameter of the system. One can already anticipate the relevance of this observation to the stability of the contact line. If the instability is controlled by the size of the ridge, then hydro-

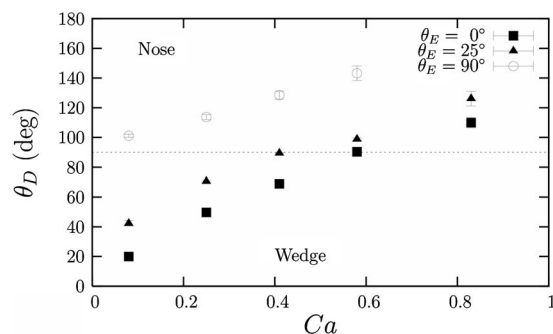


FIG. 4. Dynamic contact angle as a function of Ca .

phobic substrates will, in general, give rise to unstable fronts, while the opposite will be expected for hydrophilic substrates.

B. Inclined substrates

To study the effect of the inclination angle ($D \neq 0$) on the shape of the front we perform runs at five inclination angles for $\theta_E=90^\circ$ at fixed Ca . Figure 6 shows stationary profiles for these runs. The main effect of decreasing the inclination angle is to flatten the profile. In turn, the dynamic contact angle decreases with decreasing α .

We extend our simulations for various Ca and θ_E values. Figure 5 shows plots of h_{\max}/h_c as a function of Ca for each α and θ_E considered. The effect of wetting properties is diminished as the inclination angle increases. For very small α , $h_{\max}/h_c \rightarrow 1$, regardless of the capillary number and equilibrium contact angle. Figure 7 shows plots of the excess contact angle, $\theta_D - \theta_E$, as a function of Ca . In all cases the contact angle increases with increasing force, as expected. The slope of the plots decreases for large Ca , indicating that the contact angle saturates to a limiting value. The effect of decreasing the inclination angle is to make the excess contact angle smaller for a given Ca value.

VI. LINEAR STABILITY ANALYSIS

Having explored the effect of wetting properties in the unperturbed front, we explore how these affect the evolution of a slightly perturbed contact line. Here, simulation parameters are chosen so the dynamic contact angle lies not only in the hydrophilic regime, but also in the hydrophobic and superhydrophobic regimes, which have not been studied previously.

TABLE I. Simulation parameters for runs presented in Fig. 3.

Run	$\theta_E=0^\circ$		$\theta_E=25.2^\circ$		$\theta_E=90^\circ$			
	Ca	$\theta_D(^\circ)$	Run	Ca	$\theta_D(^\circ)$	Run	Ca	$\theta_D(^\circ)$
(a)	0.08	19.9	(f)	0.08	42.4	(k)	0.08	101.1
(b)	0.25	49.7	(g)	0.25	70.6	(l)	0.25	113.6
(c)	0.41	68.9	(h)	0.41	89.4	(m)	0.28	128.0
(d)	0.58	90.3	(i)	0.58	98.8	(n)	0.41	128.5
(e)	0.83	110.0	(j)	0.83	126.1	(o)	0.58	143.2

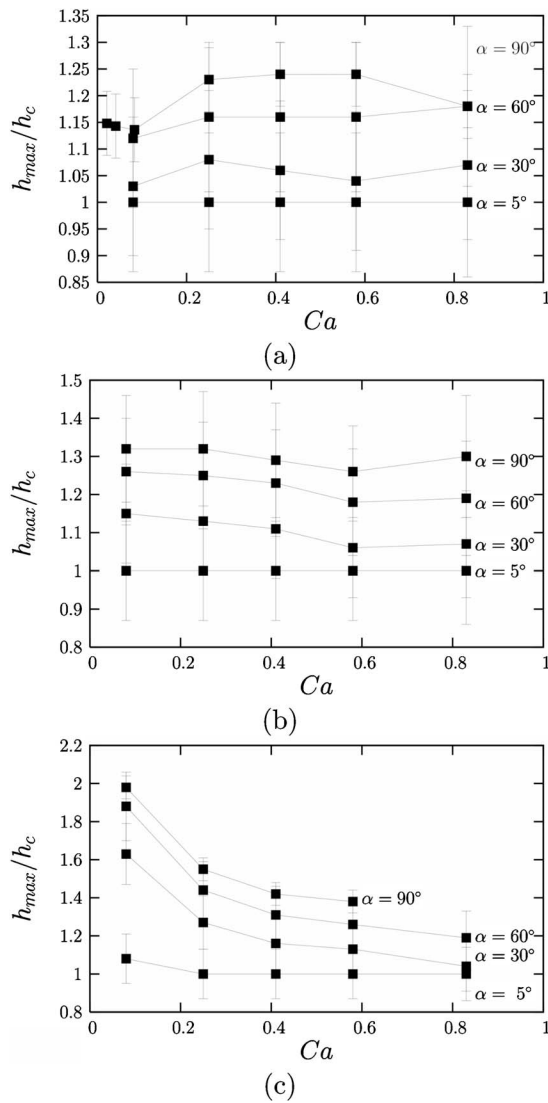


FIG. 5. Maximum film thickness as a function of Ca . (a) $\theta_E=0^\circ$. (b) $\theta_E=25^\circ$. The results are presented explicitly for α and Ca , as h does not scale with the lubrication parameter D . (c) $\theta_E=90^\circ$.

Front destabilization occurs by virtue of a spatial variation of the capillary ridge. When the front is perturbed transversely (see Fig. 1), the ridge at the troughs of the perturbation relaxes due to capillarity, generating transverse flows that feed the peaks. As a consequence, the peaks increase their local thickness and, in turn, their velocity. This is countered by surface tension, which tends to flatten the perturbed contact line. For long wavelengths surface tension is outweighed by the driving force and the front destabilizes.

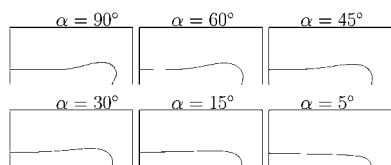


FIG. 6. Height profiles for varying inclination angle at $Ca=0.41$ and $\theta_E=90^\circ$.

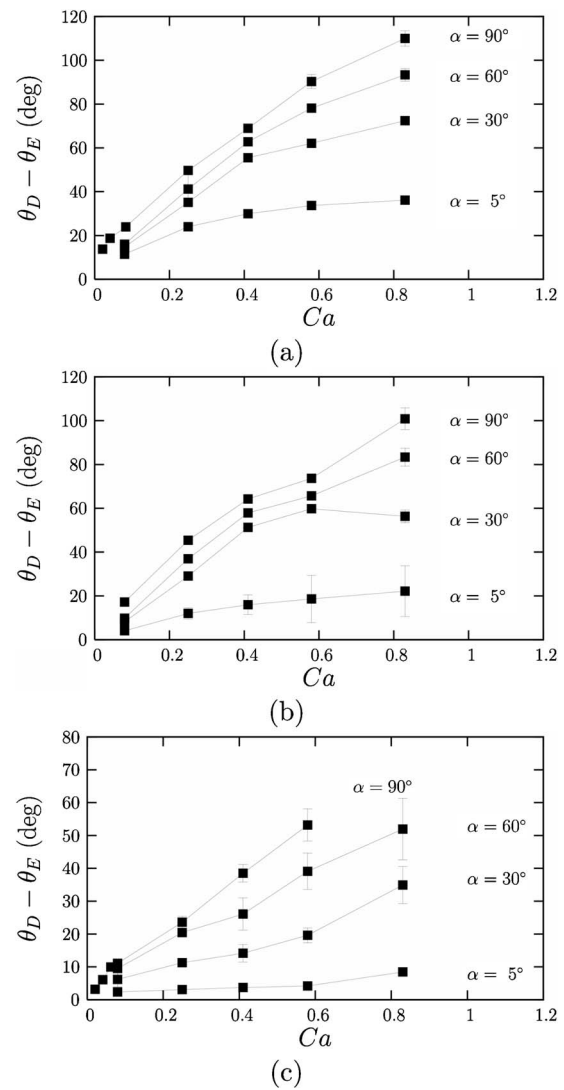


FIG. 7. Excess dynamic angle (with respect to equilibrium contact angle) as a function of Ca . (a) $\theta_E=0^\circ$. (b) $\theta_E=25^\circ$. (c) $\theta_E=90^\circ$.

A. Vertical substrates

We first consider a vertical substrate and explore the dynamics for five different equilibrium contact angles: $\theta_E=0^\circ$, $\theta_E=25^\circ$, $\theta_E=60^\circ$, $\theta_E=75^\circ$, and $\theta_E=90^\circ$ at $Ca=0.41$. In steady state, the dynamic contact angle for each substrate is $\theta_D=71^\circ$, $\theta_D=78^\circ$, $\theta_D=97^\circ$, $\theta_D=106^\circ$, and $\theta_D=128^\circ$, respectively. For a given steady front, we impose a single-mode perturbation to the contact line, $x_P=x_U+\delta\cos(ky)$, where x_U and x_P are the unperturbed and perturbed x -coordinates of the contact line, respectively, k is the perturbation mode, and δ the perturbation amplitude. In the linear regime, $\delta\sim\exp(\omega t)$, where ω is the growth rate of the perturbation. To estimate ω we measure δ as a function of time and perform a linear fit to the $\log(\delta)-t$ data.

Figure 8(a) shows plots of ω/ω_c as a function of k/k_c , where $\omega_c=1/t_c$ and $k_c=1/x_c$ are the characteristic scales of the problem. For each angle, there exists a band of unstable modes, which broadens as one increases θ_D . There is hence a clear dependence of the stability of the front on the wetting properties of the solid. Nevertheless, the qualitative form of

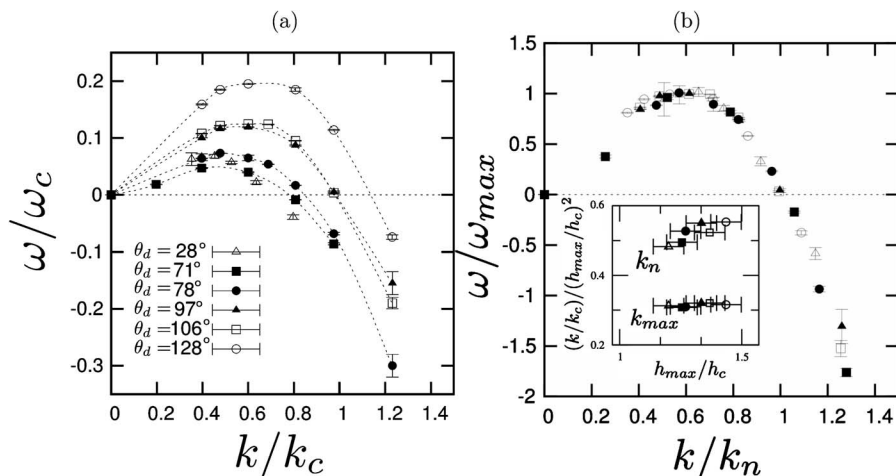


FIG. 8. (a) Dispersion relation curves for fronts with different θ_E and Ca. (b) Collapsed dispersion relations. Inset: first unstable mode and maximum unstable mode scalings with the maximum film thickness. (Δ): Ca=0.041, $\theta_E=0^\circ$; (\blacksquare): Ca=0.41, $\theta_E=0^\circ$; (\bullet): Ca=0.41, $\theta_E=25^\circ$; (\blacktriangle): Ca=0.41, $\theta_E=60^\circ$; (\square): Ca=0.41, $\theta_E=75^\circ$; (\circ): Ca=0.41, $\theta_E=90^\circ$.

the dispersion relation remains the same for all substrates. In Fig. 8(b) we scale the dispersion relations, scalings being $\omega \rightarrow \omega/\omega_{\max}$ and $k \rightarrow k/k_n$. Here ω_{\max} and k_n are the maximum growth rate and the first unstable mode of each dispersion relation. The collapse is remarkably good. We draw as a conclusion that the stability of wedge- and nose-shaped fronts is determined by the same mechanism. Given that the instability is driven by gravity, thicker ridges should lead to a wider band of unstable modes and a larger growth rate. This is consistent with the fact that the size of the ridge, h_{\max} , is larger for hydrophobic substrates at fixed Ca as explained in Sec. V (see Fig. 3). A signature of this effect can be appreciated in the inset of Fig. 8(b), where we plot $(k_{\max}/k_c)/(h_{\max}/h_c)^2$ and $(k_n/k_c)/(h_{\max}/h_c)^2$ as a function of $(h_{\max}/h_c)^2$. Using this scaling, the most unstable mode shows no dependence on h_{\max} , a condition that can only be fulfilled if $(k_{\max}/k_c) \sim (h_{\max}/h_c)^2$. Hence, as the size of the capillary ridge increases, the front has a smaller most unstable wavelength.

Previous results obtained by Spaid and Homsy¹² correspond to the $Ca \ll 1$ (and therefore $\theta_D \ll 1$) limit. To regularize the contact line singularity they introduce a slip length at the solid, which affects the stability of the front. For $\tan(\theta_D) < 0.1$ they find a most unstable mode $k_{\max}/k_c = 0.5$, the corresponding growth rate lies approximately in the range of $0.05 \leq \omega_{\max}/\omega_c \leq 0.2$, and a first unstable mode in the range of $0.7 \leq k_n/k_c \leq 0.9$. In their simulations, larger ω_{\max} and smaller k_n are observed as the slip length becomes small. To recover these results we fix $\theta_E = 0^\circ$ and $Ca = 0.041$. The dynamic contact angle of the steady front is $\theta_D = 28^\circ$. The resulting dispersion relation is shown in Fig. 8(a) and should be compared to the one corresponding to $\theta_D = 71^\circ$ which was done at $Ca = 0.41$ and equal θ_E . The main effect of decreasing the capillary number is to increase the growth rate of the perturbation. This is because the size of the ridge (here given by its width) is typically larger for small Ca [see Figs. 3(a)–3(e)]. For $Ca = 0.041$ we obtain $k_{\max}/k_c \approx 0.5$, $k_n/k_c \approx 0.7$ and a maximum growth rate $\omega_{\max}/\omega_c \approx 0.07$. These values agree with those reported by Spaid and Homsy. Hence our results converge to the lubrication theory results at low

Ca. As expected, this low-Ca dispersion relation is qualitatively equal to the rest as it collapses to the same universal curve shown in Fig. 8(b).

B. Inclined substrates

We now consider the effect of the substrate inclination angle. We fix $\theta_E = 90^\circ$ and $Ca = 0.41$ and consider five inclination angles, $\alpha = 60^\circ$, $\alpha = 45^\circ$, $\alpha = 30^\circ$, $\alpha = 15^\circ$, and $\alpha = 5^\circ$. As shown in Fig. 6, the profile gradually flattens as the inclination angle is decreased. For $\alpha = 5^\circ$ the bump disappears completely. Dispersion relations for each front are shown in Fig. 9. The effect of the normal force, in agreement with previous results,^{11,13} is to suppress the instability. Indeed, for $\alpha < 15^\circ$ all wavelengths considered are stable. The maximum height of the front at this inclination angle is $h_{\max}/h_c \approx 1.1$.

The critical inclination angle for the front destabilization is expected to increase for wetting fluids. To illustrate this effect, consider, for instance, the low-Ca region of the maximum height plots shown in Figs. 5(a)–5(c) for, say, $\alpha = 30^\circ$. At this inclination angle and for $Ca = 0.08$, we have $h_{\max}/h_c = 1.02$, $h_{\max}/h_c = 1.15$, and $h_{\max}/h_c = 1.63$ for $\theta_E = 0^\circ$, $\theta_E = 25^\circ$, and $\theta_E = 90^\circ$, respectively. Therefore, the front should

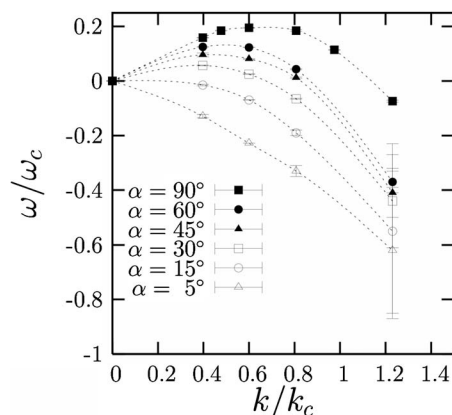


FIG. 9. Dispersion relation for varying substrate inclination angle at $Ca = 0.41$ and $\theta_E = 90^\circ$.

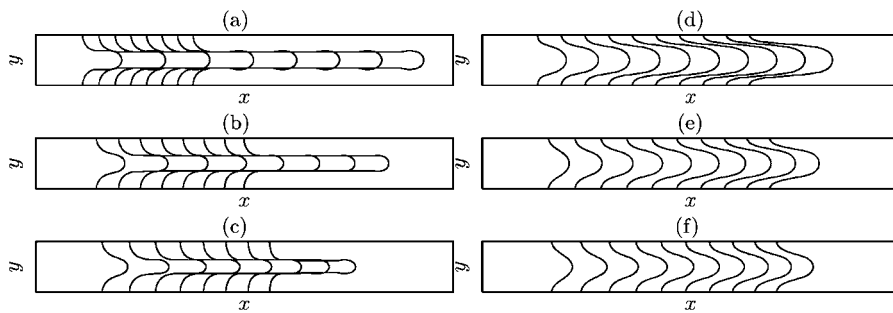


FIG. 10. Interface profiles at different contact angles and capillary numbers. Parameters for each run are summarized in Table II.

be stable for $\theta_E=0^\circ$ as the height approaches the limiting value $h/h_c \rightarrow 1$. For $\theta_E=25^\circ$, the ridge must be marginally unstable, given that the bump size is close (and above) the threshold value obtained for $\theta_E=90^\circ$. For $\theta_E=90^\circ$, the front must be unstable. Therefore, the critical destabilization angle increases as θ_E decreases. From Fig. 5, the critical inclination angle to destabilize the front at $\theta_E=0^\circ$ is $\alpha_c \approx 60^\circ$.

VII. NONLINEAR DYNAMICS

A. Sawtooth and finger patterns

Having explored the linear stability of the front, we address the long time behavior of the instability for the case of a single mode. We are interested in the effect of the wetting properties on the emerging patterns. We consider four equilibrium contact angles, namely, $\theta_E=25^\circ$, $\theta_E=60^\circ$, $\theta_E=75^\circ$, and $\theta_E=90^\circ$. For each contact angle, we consider domains of a size comparable to the most unstable wavelength predicted by the linear stability analysis.

1. Vertical substrates

We start by considering vertical substrates. For each equilibrium contact angle we perform runs at different Ca. After the destabilization of the contact line, we observe a transient in which a single pattern emerges. Eventually, the pattern acquires a steady shape and propagates with constant velocity.

In Fig. 10 we show the evolution of contact line profiles for $\theta_E=25^\circ$ and $\theta_E=90^\circ$ at different capillary numbers. The evolution of the interface for angles in between is similar. Runs (a)–(c) in the figure correspond to $\theta_E=90^\circ$ and increasing Ca. They exhibit a finger pattern that propagates at constant velocity. Wider patterns are obtained for runs (d)–(f), which correspond to $\theta_E=25^\circ$ and increasing Ca. Of these,

runs (d) and (e) evolve toward a steady finger at long times, while run (f) saturates to a steady length. This corresponds to the sawtooth shape reported in previous studies.^{7,8,13}

Table II summarizes Ca values for each of these runs. It is clear from the data that the pattern is not entirely determined by Ca, as both wide and thin patterns are observed for the same range in Ca. To characterize these patterns we measure their length L defined as the distance between the minimum (base) and maximum (tip) x -coordinates of the contact line. From Fig. 10, L is strongly affected by the wetting properties of the fluid. In Fig. 11 we show plots of L as a function of time for runs (a)–(f). For runs (a)–(c), the time variation of L is larger than for runs (d)–(f). In fact, for run (f), L is constant over time, meaning that the sawtooth pattern saturates to a given length in the nonlinear regime. To quantify this effect we measure the growth rate \dot{L} , which we summarize in Table II. For both equilibrium contact angles, the growth rate decreases as Ca increases.

Figure 12 shows three-dimensional plots of the free surface when the \dot{L} has reached a constant value. We observe that larger patterns are obtained when the difference between the size of the capillary ridge at the tip and the base is also large. From lubrication theory, the local velocity is expected to be $u \sim h_{\max}(y)^2$ and hence $\dot{L}(t_c/x_c) \sim \Delta$, with $\Delta = [h_{\max}(y_A)^2 - h_{\max}(y_B)^2]/h_c^2$. Here, subscripts A and B stand for the positions of the tip and the base of the pattern (see Fig. 1), Fig. 13 shows a plot of $\dot{L}(t_c/x_c)$ as a function of Δ . The growth rate follows a single curve when plotted as a function of this quantity, regardless of the capillary number and equilibrium contact angle. Below a threshold value, Δ_0

TABLE II. Simulation parameters and pattern growth rate for vertical substrates.

Run	θ_E (deg)	Ca	$\dot{L}(t_c/x_c)$
(a)	90	0.21	0.82
(b)	90	0.41	0.45
(c)	90	0.83	0.14
(d)	25	0.41	0.12
(e)	25	0.83	0.04
(f)	25	1.65	0.00

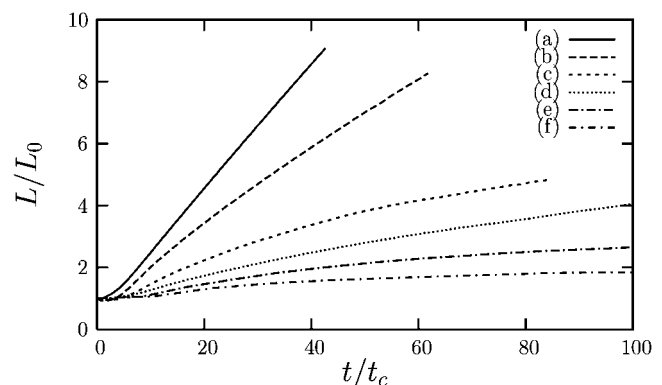


FIG. 11. Pattern length as a function of time. Letter keys correspond to parameters shown in Table II. (a)–(c) $\theta_E=90^\circ$ and increasing Ca; (d)–(f) $\theta_E=25^\circ$ and increasing Ca.

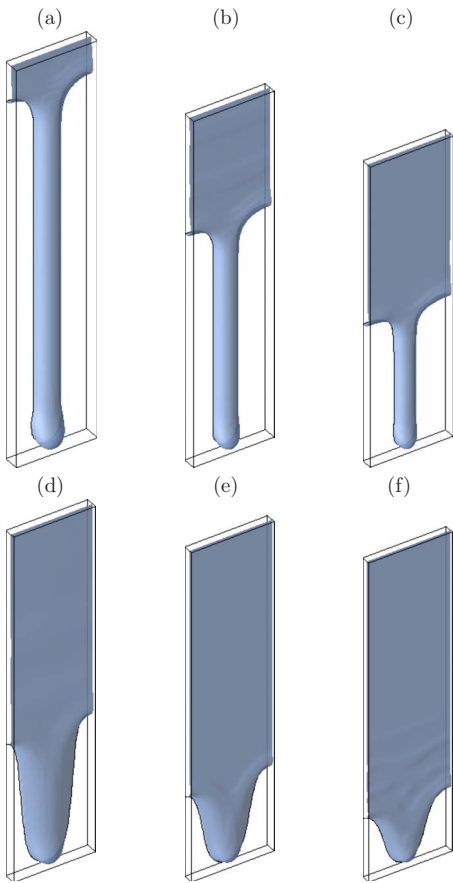


FIG. 12. (Color online) Interface profiles at different contact angles and capillary numbers. Parameters for each run are summarized in Table II.

$=0.33 \pm 0.09$, the growth rate vanishes, meaning that the amplitude of the pattern saturates while there is still a finite difference of the ridge thickness between its tip and its base. This effect is a consequence of the balance between surface tension, which tends to flatten the contact line and the uneven mass distribution caused by the instability.

2. Inclined substrates

We now study the effect of the inclination angle in the shape of the pattern. We consider $\theta_E=90^\circ$ and $Ca=0.41$ and perform simulations at $\alpha=90^\circ$, $\alpha=60^\circ$, and $\alpha=45^\circ$. Figure 14 shows the evolution of the contact line as α is varied. The effect of decreasing α is to decrease the growth rate and to

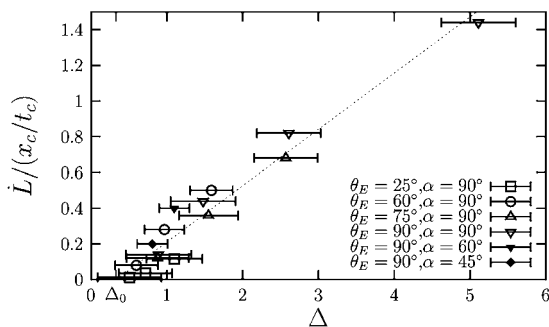


FIG. 13. Pattern growth rate as a function of the difference of the squared film thickness measured at the tip and the base of the pattern.

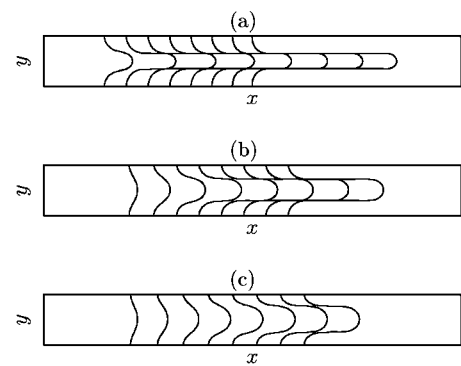


FIG. 14. Interface profiles at different inclination angles. (a) $\alpha=90^\circ$, (b) $\alpha=60^\circ$, and (c) $\alpha=45^\circ$.

increase the width of the pattern. The relevant effect of α is to flatten the free surface, a situation that is also attained by increasing substrate wettability. Hence, the inclination angle and substrate wettability have similar effects. Indeed, the pattern growth rate in these runs falls in the same curve when plotted against Δ , as shown in Fig. 13.

B. Finger dynamics

In the following we investigate whether the same finger solution is always observed regardless of the initial state of the system. We first examine the evolution of various initial conditions composed of a single mode. Next we consider the evolution of a multiple mode perturbation, where the most unstable mode is expected to dominate the dynamics according to linear stability results. Finally, we examine the effect of the system size. To compare results in this section to the single finger solution parameters values are fixed according to run (d) in Table II, which corresponds to a finger in the hydrophobic regime.

1. Effect of initial conditions

We consider a system of size $W \approx \Lambda_{max}$, where Λ_{max} is the most unstable wavelength according to the linear stability analysis. Initial conditions are fixed as (i) a single-mode perturbation with $\Lambda=W$, (ii) a parabolic perturbation, and (iii)–(v) a fingerlike perturbation with initial finger widths $\lambda=0.45$, $\lambda=0.63$, and $\lambda=0.80$, respectively, where λ is measured in units of the system size. The evolution of the contact line is depicted in Fig. 15. Run (i) shows the evolution of the $\Lambda=W$ perturbation, which grows and saturates to the finger pattern. The next four cases [(ii)–(v)] show all the same type

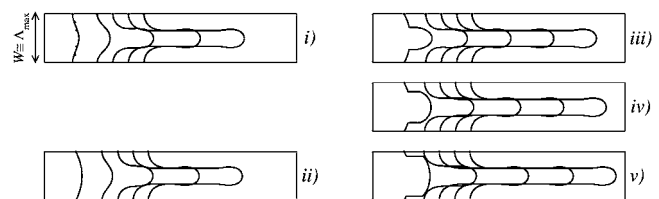


FIG. 15. Contact line evolution for different initial conditions: (i) Sinusoidal perturbation; (ii) parabolic perturbation; (iii)–(v) fingerlike perturbation with finger widths $\lambda=0.45$, $\lambda=0.63$, and $\lambda=0.80$ (in units of the width of the system).

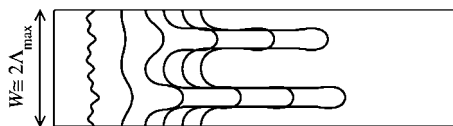


FIG. 16. Contact line evolution for a perturbation composed of four modes.

of evolution. The interface rapidly relaxes from its initial configuration at the early times of the simulation and saturates to a finger pattern, which for all cases has the same finger width and pattern growth rate as that from the run (d) in Table II. These results indicate that the stationary solution is not sensitive to initial conditions.

For a perturbation composed of more than one mode we expect that the most unstable wavelength dominates the dynamics, according to linear stability results. We consider a system of width $W \approx 2\Lambda_{\max}$ and an initial perturbation composed of four modes. Corresponding wavelengths are $\Lambda = W$, $\Lambda = W/2$, $\Lambda = W/4$, and $\Lambda = W/8$, of which $\Lambda = W/2$ is expected to grow faster than the rest. The amplitude is set to a small value (about two lattice spacings) with random deviations uniformly distributed. As shown in Fig. 16, all wavelengths except for $\Lambda = W/2$ rapidly decay. The dominant mode then grows until a two-finger solution is obtained. Each of the fingers turns out to be identical to the single finger solution obtained for run (d), their length being dictated by initial conditions.

2. Effect of system size

We next focus on the effect of the system size in the observed pattern. We consider four system sizes, $W = \Lambda_{\max}$, $W = 3\Lambda_{\max}/2$, $W = 2\Lambda_{\max}$, and $W = 3\Lambda_{\max}$. For $W = \Lambda_{\max}$ we fix a two-finger initial condition, while for all other runs we fix a single-mode perturbation of wavelength $\Lambda = W$. Figure 17(a) shows the evolution of the contact line for the two-finger initial condition. Even though the amplitude of both fingers is large, the system size allows only the growth of one finger. After a transient in which the shorter finger declines, the expected one-finger solution is thus recovered.

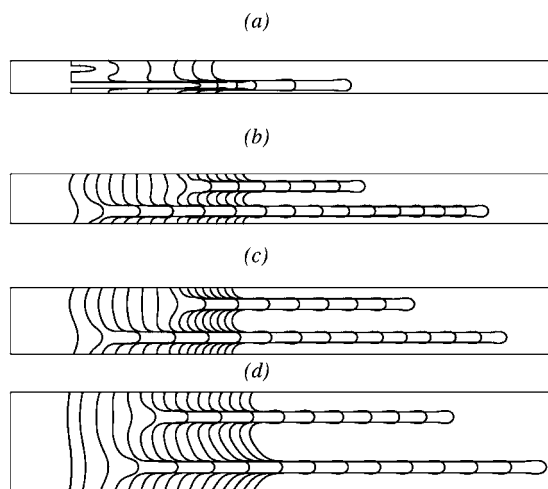


FIG. 17. Contact line evolution for different system sizes. (a) $W = \Lambda_{\max}$, (b) $W = 3\Lambda_{\max}/2$, (c) $W = 2\Lambda_{\max}$, and (d) $W = 3\Lambda_{\max}$.

Figures 17(b) and 17(c) show the evolution of the contact line for $W > \Lambda_{\max}$. Even though a single mode was present at the initial condition, the system evolves and additional modes emerge. In all cases, two-finger stationary solutions are obtained. Fingers have the same shape, width, and growth rate as the single finger solution. Nonetheless, the distance between fingers varies sensibly with increasing system size. Such a dispersion in pattern spacing is in agreement with early observations by de Bruyn,³ who reported deviations of as much as 25% in his measurements. This was later confirmed by Kondic and Diez,¹³ who pointed out that growing fingers interact depending on the initial conditions, thus generating steady patterns spaced with a certain degree of dispersion. Fingers grow whenever a sufficient amount of mass is available, i.e., when the separation between fingers lies in the band of unstable wavelengths given by linear stability.

VIII. DISCUSSION AND CONCLUSIONS

The flow of forced thin films on dry inclined substrates has been investigated for different substrate wettabilities, as well as for a wide range of inclination angles at large capillary numbers. Film dynamics explored in this work range from the hydrophilic to the superhydrophobic regimes.

Our results indicate that the stability of the contact line is influenced by the wetting properties of the solid. Wedge shaped fronts are generally more stable than nose-shaped ones. However, the stability of noses and wedges remains qualitatively the same, as all dispersion relations collapse to a single curve. The reason for this universal behavior lies in the fact that the main role of wetting properties is to fix the size of the capillary ridge, which is the relevant parameter for the stability of the front. The more hydrophobic the substrates the larger the ridge size. Then, hydrophobic substrates tend to destabilize the front. The size of the ridge can also be controlled via the inclination angle of the substrate. Accordingly, wider bands of unstable modes are observed for large inclination angles. For inclined substrates, the normal component of gravity stabilizes the film for completely wetting fluids, in agreement with previous studies.^{13,14} This effect is observed for partially wetting and nonwetting fluids as well.

The longtime evolution of the instability gives rise to the growth of two types of pattern; either sawtooth shaped patterns or finger shaped ones are observed. The substrate wetting properties and inclination angle have a role in the determination of the type of pattern. Fingers are observed at either hydrophobic substrates or large inclination angles, while the opposite is found for the sawtooth pattern. A direct connection with size of the capillary ridge then follows. Hydrophobic substrates and large inclination angles favor the formation of large capillary ridges. In such case, surface tension is not enough to balance the driving force given by the weight of the ridge along the contact line. Therefore, a finger develops. On the other hand, when the substrate is hydrophilic or the inclination angle is small, the size of the ridge becomes small accordingly. Surface tension then balances the driving force in the nonlinear regime, thus giving rise to a saturated sawtooth pattern. Indeed, we find that all growth rates are

parametrized by the difference of the size of the ridge between the base and the tip of the pattern.

The robustness of the finger solution is studied. We have found that for a given choice of Ca , α , and θ_E , the same finger solution is obtained, regardless of the initial condition and system size. Fingers grow whenever a sufficient mass reservoir is available, i.e., whenever the separation between them is comparable to the most unstable wavelength predicted by linear stability.

ACKNOWLEDGMENTS

We acknowledge financial support from Dirección General de Investigación (Spain) under Project Nos. FIS 2006-12253-C06-05 and FIS 2005-01299. R.L.-A. wishes to acknowledge support from CONACyT (México) and Fundación Carolina (Spain). I.P. thanks Distinció from DURSI (Generalitat de Catalunya). The authors thankfully acknowledge the computer resources, technical expertise, and assistance provided by the Barcelona Supercomputing Center—Centro Nacional de Supercomputación.

¹P.-G. de Gennes, F. Brochard-Wyart, and D. Quéré, *Capillarity and Wetting Phenomena: Drops, Bubbles, Pearls and Waves* (Springer-Verlag, New York, 2003).

²P. de Gennes, “Wetting: statics and dynamics,” *Rev. Mod. Phys.* **57**, 827 (1985).

³K. Holloway, P. Habdas, N. Semsarillar, K. Burfitt, and J. de Bruyn, “Spreading and fingering in spin coating,” *Phys. Rev. E* **75**, 046308 (2006).

⁴O. Kuksenok, D. Jasnow, J. Yeomans, and C. Balazs, “Periodic droplet formation in chemically patterned microchannels,” *Phys. Rev. Lett.* **91**, 108303 (2003).

⁵H. Song, J. Tice, and F. Ismagilov, “A microfluidic system for controlling reaction networks in time,” *Angew. Chem., Int. Ed.* **42**, 767 (2003).

⁶K. Hosokawa, T. Fujii, and I. Endo, “Handling of picoliter liquid samples in a poly(dimethylsiloxane)-based microfluidic device,” *Anal. Chem.* **71**, 4781 (1999).

⁷N. Silvi and E. Dussan, “On the rewetting of an inclined solid surface by a liquid,” *Phys. Fluids* **28**, 5 (1985).

⁸J. Jerret and J. de Bruyn, “Fingering instability of a gravitationally driven contact line,” *Phys. Fluids A* **4**, 234 (1991).

⁹M. P. Brenner, “Instability mechanism at driven contact lines,” *Phys. Rev. E* **47**, 4597 (1993).

¹⁰S. M. Troian, E. Herbolzheimer, S. A. Safran, and J. Joanny, “Fingering instabilities in driven spreading films,” *Europhys. Lett.* **10**, 25 (1989).

¹¹A. L. Bertozzi and M. P. Brenner, “Linear stability and transient growth in driven contact lines,” *Phys. Fluids* **9**, 530 (1997).

¹²M. Spaid and G. Homsy, “Stability of Newtonian and viscoelastic dynamic contact lines,” *Phys. Fluids* **8**, 460 (1996).

¹³L. Kondic and J. Diez, “Pattern formation in the flow of thin films down an incline: Constant flux configuration,” *Phys. Fluids* **13**, 3168 (2001).

¹⁴D. T. Moyle, M.-S. Chen, and G. Homsy, “Nonlinear rivulet dynamics during unstable wetting flows,” *Int. J. Multiphase Flow* **25**, 1243 (1999).

¹⁵I. Veretennikov, A. Indeikina, and H.-C. Chuang, “Front dynamics and fingering of a driven contact line,” *J. Fluid Mech.* **373**, 81 (1998).

¹⁶V. M. Kendon, M. E. Cates, I. Pagonabarraga, J. C. Desplat, and P. Bladon, “Inertial effects in three-dimensional spinodal decomposition of a symmetric binary mixture: a Lattice-Boltzmann study,” *J. Fluid Mech.* **440**, 147 (2001).

¹⁷K. Stratford, J.-C. Desplat, P. Stansell, and M. E. Cates, “Binary fluids under steady shear in three dimensions,” *Phys. Rev. E* **76**, 030501 (2007).

¹⁸A. Briant and J. Yeomans, “Lattice Boltzmann simulations of contact line motion. II. Binary fluids,” *Phys. Rev. E* **69**, 031603 (2004).

¹⁹R. Ledesma-Aguilar, A. Hernández-Machado, and I. Pagonabarraga, “Three-dimensional aspects of fluid flows in channels: I. Meniscus and thin film regimes,” *Phys. Fluids* **19**, 102112 (2007).

²⁰R. Ledesma-Aguilar, I. Pagonabarraga, and A. Hernández-Machado, “Three-dimensional aspects of fluid flows in channels: II. Effects of meniscus and thin film regimes in viscous fingers,” *Phys. Fluids* **19**, 102113 (2007).

²¹J. C. Desplat, I. Pagonabarraga, and P. Bladon, “Ludwig: A parallel Lattice-Boltzmann code for complex fluids,” *Comput. Phys. Commun.* **134**, 273 (2001).

²²A. Bray, “Theory of phase ordering-kinetics,” *Adv. Phys.* **43**, 357 (1994).

²³A. Ladd and R. Verberg, “Lattice-Boltzmann simulations of particle-fluid suspensions,” *J. Stat. Phys.* **104**, 1191 (2001).

²⁴The interfacial profile next to the solid is distorted due to the fluid/solid interaction. As a result, the real contact line position differs from the apparent macroscopic one. This behavior is analogous, in the context of our mesoscopic approach, to the development of a precursor film due to van der Waals interactions in real fluids.